The key role of the A-site composition of oxy-hydroxyapatites in high-temperature solid–gas exchange reactions

Sophie Guillou, Nathalie Douard, Solène Tadier, Laurent Gremillard, Didier Bernache-Assollant, David Marchat

The key role of the A-site composition of oxy-hydroxyapatites in high-temperature solid–gas exchange reactions

This article has been published in
Journal of Thermal Analysis and Calorimetry (2022) Vol. 147, pp. 13135–13150
https://doi.org/10.1007/s10973-022-11512-3

S. Guillou[a], N. Douard[a], S. Tadier[b], L. Gremillard[b], D. Bernache-Assollant[a], D. Marchat[a]

[a] Mines Saint-Etienne, Univ Lyon, Univ Jean Monnet, Etablissement Français du Sang, INSERM, U1059 Sainbiose, 42023, Saint-Étienne, France
[b] Univ Lyon, CNRS, INSA Lyon, UCBL, MATEIS, UMR5510, Villeurbanne 69100, France
* Corresponding authors : Douard@emse.fr

Abstract
The manufacture of carbonated hydroxyapatite-based bioceramics with control of the composition and microstructure remains challenging and reveals our lack of knowledge regarding the thermal behavior of such materials, particularly at high temperatures under reactive atmospheres. This work lays a foundation for addressing this issue by investigating the solid–gas exchange reactions occurring between oxy-hydroxyapatites (O_xHA) and a CO_2-rich atmosphere during thermal treatment. Accordingly, O_xHA reference powders with different oxygen contents ($0 \le x \le 0.79$) were produced, extensively characterized and heat-treated under a CO_2-rich atmosphere at 950 °C for 5 h. The results of physicochemical, thermal and microstructural analyses showed that the A-site composition of O_xHA controls the exchange reactions: a high initial OH content induced concomitant A-site dehydration and carbonation; conversely, a high OH vacancy content induced A-site hydration as a first step. Furthermore, the specific surface area significantly influenced the solid–gas exchange reactions by controlling their kinetic.

Keywords
A-type carbonated hydroxyapatite, Oxy-hydroxyapatite, Thermogravimetric analysis, Solid–gas exchange reactions, Kinetic

1 Introduction
In the field of critical-size bone defect healing, current therapeutic solutions (e.g., bone grafting with human, animal, or natural materials or bone replacement with synthetic materials) remain challenging [1]. Calcium phosphate materials, such as stoichiometric hydroxyapatite (HA, $Ca_{10}(PO_4)_6(OH)_2$) and tricalcium phosphate (TCP, $Ca_3(PO4)_2$), have been clinically implanted for more than 30 years [1] but still do not satisfy the requirements for large bone defects [2]. These materials display relatively poor osteoinductive properties [3, 4], and their biodegradation rate cannot support the development of newly formed bone [5, 6].
Because of these limitations, efforts have focused on the processing of new synthetic bioinspired implants [7, 8]. In line with this current trend, carbonated hydroxyapatites (CHAs) stand out because of their high similarity with natural bone minerals, whose composition can be approximated as $Ca_{8.3}(PO_4)_{4.3}(HPO_4)_{0.7}(CO_3)_{1.0}(OH)_{0.15}(CO_3)_{0.07}$ [9, 10]. CHAs can create functional interfaces with natural bone [11, 12] and induce high rates of bone formation [13], and their degradation products are naturally metabolized by cells [14]. Moreover, their biodegradation rate is greater than that of HA and is related to their carbonate ion content [4, 5, 15,16,17,18]. This particular property allows for patient-specific implants with customized biodegradation rates.
Carbonate ions can be located at both the hydroxyl (A-site) and phosphate (B-site) structural sites of HA. A-site carbonate-for-hydroxyl substitution results from a thermally activated reaction between the apatite structure and a CO_2-rich atmosphere according to Eq. (1) (the Kröger–Vink notation is defined in Table 1) [19,20,21].

$$CO_2^{(g)} + 2OH_{OH}^{X} = CO_3'_{\ OH} + V_{OH}^{o} + H_2O^{(g)} \qquad (1)$$

Table 1. Kröger–Vink notation

Notation	Ion/structural location	Net electronic charge
OH_{OH}^{X}	OH^- ion in the OH structural location	Neutral charge
O'_{OH}	O^{2-} ion in the OH structural location	Single negative charge
$CO'_{3\ OH}$	CO_3^{2-} ion in the OH structural location	Single negative charge
V_{OH}^{o}	Vacancy in the OH structural location	Single positive charge

A-type CHA bioceramics (C_AHA, $Ca_{10}(PO_4)_6(OH)_{2-2a}(CO_3)_a$ with $0 \le a \le 1$) showed a biological response either lower than or, at best, equal to that of HA in terms of osteoblast adhesion and proliferation [17, 21, 22].

To the best of our knowledge, the improved biological properties of CHA can be attributed to B-type CO_3^{2-} ions. B-site CHA (C_BHA, $Ca_{10-b}(PO_4)_{6-b}(CO_3)_b(OH)_{2-b}$ with $0 \le b \le 2$ [23]) powders are synthesized via aqueous precipitation by mixing calcium, phosphate and carbonate solutions under controlled temperature, pH and atmosphere conditions. Even though this synthetic route is well known [24,25,26], manufacturing C_BHA bioceramics remains challenging. Sintering must be carried out under a CO_2-rich atmosphere to prevent thermal decomposition [23, 27], leading to an enrichment of CO_3^{2-} ions in the A-sites and therefore to A/B-type CHAs ($C_{A/B}HA$). This chemical modification can alter the bioceramic biodegradation rate and potentially reduce its biological potential. In addition, the presence of CO_3^{2-} ions in the A-sites has been shown to hinder densification [28]. Sufficient consolidation of $C_{A/B}HA$-based bioceramics thus requires a higher sintering temperature or longer sintering dwell time, which may be accompanied by thermal decomposition or grain growth. Control of the pore density and size at the submicron scale, which is key to promoting revascularization [29] and osteoclastogenesis [30, 31], can then become an issue. As a result, this carbonate-for-hydroxyl substitution in the apatite lattice, induced by sintering under a CO_2-rich atmosphere, affects both the final composition and the microstructural features of CHA-based bioceramics. As the interactions between an implant and host cells highly depend on both of these properties [2, 32-34], this carbonate-for-hydroxyl substitution must be carefully controlled. However, no investigation of such solid–gas exchange reactions is available in the literature. This study aims to provide insight into the solid–gas exchange reactions occurring between oxy-hydroxyapatites (O_xHA, $Ca_{10}(PO_4)_6(OH)_{2-2x}O_x$ with x ranging from 0 to 0.79) and a CO_2-rich atmosphere during thermal treatments. This O_xHA-CO_2 model constitutes a first step toward understanding the mechanism(s) of the exchange reactions between CO2 gas and A-sites before switching to models that are more complex such as $C_{A/B}HA$. The parameters likely to affect these reactions are mainly the powder intrinsic features and the heat treatment parameters. This work focuses on the influence of the initial A-site chemical composition (x in O_xHA) and the specific surface area (SSA). O_xHA reference samples with different or equivalent SSAs were produced through heat treatment of a stoichiometric HA powder under a dry atmosphere according to Eq. (2) [35, 36].

$$2OH_{OH}^{X} = O'_{OH} + V_{OH}^{o} + H_2O^{(g)} \qquad (2)$$

Special attention was given to prevent decomposition while manufacturing O_xHA [35, 37-42]. Indeed, O_xHA decomposes into a mixture of TCP and tetracalcium phosphate (TTCP, $Ca_4(PO_4)_2O$) according to Eq. (3) when the A-site vacancy is above 0.8 [36, 43].

$$Ca_{10}(PO_4)_6(OH)_{2-2x}O_x = 2Ca_3(PO_4)_2 + Ca_4(PO_4)_2O + (1-x)H_2O^{(g)} \qquad (3)$$

with $0 < x < 1$.

The solid–gas exchange reactions occurring between the O_xHA samples and a CO_2-rich atmosphere were then monitored by thermogravimetric analysis. All steps of the manufacture and characterization of the samples were strictly monitored to determine the key role of the initial A-site composition of O_xHA in these solid–gas exchange reactions and to develop the associated mass balance equations.

2 Materials and methods

2.1 Sample preparation

2.1.1 Starting hydroxyapatite powder

HA powder was synthesized by a conventional aqueous precipitation method according to the procedure detailed in [25]. A diammonium hydrogen phosphate aqueous solution ($(NH_4)_2HPO_4$, 99%, Merck, Germany) was added to a calcium nitrate aqueous solution ($Ca(NO_3)_2$, $4H_2O$, 99%, Merck, Germany) under stirring. The reaction was performed under argon flow (Ar, Ar Premier, AirProducts, USA, Table 2) at a constant temperature of 65 °C and a pH of 8.0. The pH was regulated by the addition of a 28% ammonia solution (Merck, Germany) by means of a dosing pump (ProMinent, England) coupled with a pH controller and a pH sensor. The suspension was matured for 20 h and then centrifuged at 4000 rpm for 5 min (Thermo Scientific, France). The wet cakes obtained were dried at 80 °C overnight and then ground for 15 min at 150 rpm in absolute ethanol (H_3CCH_2OH, > 99.5%, VWR, Germany) by means of a planetary ball mill (PM400, Retsch, Germany) with zirconium oxide jars and balls, sieved at 25 µm (Russelfinex, Belgium), and dried at 120 °C for 24 h. The powder was finally heat-treated at 400 °C for 2 h (Carbolite, UK) under air to remove the main synthesis residues. The obtained powder is hereafter designated the raw HA powder and was found to be monophasic poorly crystallized (i.e., low local order) stoichiometric HA with remaining synthesis residues (e.g., NO_3^{2-}).

Table 2. Gas specifications: trace H2O and CO2 in Ar, He and CO2 bottle gases from AirProducts

Gas	H_2O/ppm	CO_2/ppm
Ar premier	2	0
He premier	2	0
CO_2 UltraPure	2	N.A

2.1.2 O_xHA reference samples

Hereafter, the reference samples will be designated O_xHA-s, with x indicating the O content in A-site and s indicating the specific surface area. Four O_xHA compositions were prepared with $0 \leq x \leq 0.79$.

Stoichiometric HA, i.e., O_xHA with x = 0 (O_0HA-8.6), was obtained by heating 50 g of raw HA powder in a tubular furnace (RS80, Naberthem, Germany) at 950 °C for 5 h under 72 kPa Ar and 28 kPa H_2O. This gas mixture was produced by a controlled humidity generator (WETSYS 0–200 mL·min^{-1}, Setaram Instrumentation, France) programmed to deliver gas at 60 °C with 90% relative humidity and a flow rate of 150 mL·min^{-1}. These parameters were defined after a calibration study of the WETSYS device. After the heat treatment, the powder was ground in absolute ethanol, sieved at 25 µm and dried at 120 °C for 24 h.

O_xHA samples with $x \neq 0$ were obtained by fit-for-purpose heat treatment of O_0HA-8.6 in the furnace of a thermobalance (SETSYS Evolution, Setaram Instrumentation, France) under helium flow (20 mL·min^{-1}, He Premier, AirProducts, USA, Table 2). The furnace atmosphere was 101.28 kPa He and 0.02 kPa H_2O. After loading the sample and before heating, the furnace chamber was evacuated to a pressure of 10–4 kPa. The gas flow was then activated, and an isothermal stage at 500 °C for 5 h was applied before starting the thermal ramps used for sample preparation. The heating and cooling rates were set to 10 °C·min^{-1}. The other specific parameters are detailed in "O_xHA samples" section.

Two furnace configurations were implemented. The first one aimed to record high-resolution thermogravimetric (TG) signals and consisted of batches of 70 mg using an alumina crucible of 170 µL. The second one was used to produce samples for use in a material characterization study; each batch contained 600 mg of powder placed in an alumina crucible of 1300 µL. Each sample was produced in triplicate in each furnace configuration. The isotherm dwell time in the second configuration was adjusted to obtain the same chemical composition obtained in the first configuration.

The SSA of each sample was measured in triplicate using the Brunauer–Emmett–Teller (BET) 5-point method using a N_2 adsorption isotherm (ASAP 2010, Micromeritics, Germany) after outgassing the powder at 200 °C for 5 h.

Each reference sample was stored in a desiccator to protect it from moisture prior to its characterization.

2.1.3 Carbonated samples

Four carbonated samples, hereafter denoted C-O_xHA-s, were obtained after thermal treatment of the O_xHA reference samples under a CO_2-rich atmosphere. Heat treatment was performed at 950 °C under a flow of 101.28 kPa of CO_2 (CO_2 UltraPure, AirProducts, USA, Table 2) and 0.02 kPa of H_2O in a SETSYS furnace (20 mL·min^{-1}). Before heating, the furnace chamber was evacuated to a pressure of 10^{-4} kPa. The gas flow was then activated. The heating and cooling rates were set to 30 °C·min^{-1}.
As for the reference samples, two furnace configurations were used. Each sample was produced in triplicate in both configurations. In the first configuration, 70 mg of powder was heat-treated for 5 h at 950 °C. In the second configuration, the isothermal dwell time was adjusted to obtain the same chemical composition as in the first one, starting with 600 mg of powder.

2.2 Characterization methods

2.2.1 Thermogravimetric analysis

Thermogravimetric analysis (TGA) of O_0HA-8.6 was performed in a SETSYS thermobalance from room temperature (RT) to 1300 °C at 2 °C·min^{-1} under He flow at 20 mL·min^{-1}. The TG signal was converted to the mass variation (w/w %) with respect to the initial mass of powder
filled in the crucible ($\Delta m/m_0$, Eq. (4)).

$$\frac{\Delta m}{m_0} = \frac{m_T - m_0}{m_0} \qquad (4)$$

where m_T is the sample mass at temperature T.

The TG signals recorded during the manufacture of the O_xHA samples (x > 0) were converted to the mass variation (w/w %) with respect to the mass of powder m_{500} obtained after the isothermal stage at 500 °C for 5 h ($\Delta m'/m_{500}$, Eq. (5)). The mass variation recorded until 500 °C was attributed to gas adsorption on the powder surface rather than to solid–gas exchange reactions [44, 45].

$$\frac{\Delta m'}{m_{500}} = \frac{m_T - m_{500}}{m_{500}} \qquad (5)$$

The TG signals recorded during the manufacture of carbonated samples were converted according to Eq. (4). These normalized mass variations were compared to the results obtained from different simple kinetic models using MATLAB software (R2018b, Natick, Massachusetts: The MathWorks Inc., USA).
For each TGA, a blank run was recorded using alumina powder (Al-606010, Goodfellow, England), and the blank signal was subtracted from the sample signals to reduce experimental drift. Each TGA was carried out in triplicate.

2.2.2 Physicochemical characterization

Each sample was manually ground with an agate mortar and pestle prior to physicochemical characterization.
Crystalline phases were identified by means of a D8-A25 θ/θ X-ray diffractometer (Brüker, Germany) equipped with a Lynx-Eye Position Sensitive Detector (aperture angle, 2.946°) using CuK_α radiation and operating at 40 kV and 40 mA. X-ray diffraction (XRD) patterns were collected over a 2θ range of 10–120° with angle and time increments of 0.03° and 0.6 s, respectively. The experimental patterns were compared with the reference patterns in ICDD-PDF (International Centre for Diffraction Data—Powder Diffraction Files). The lattice parameters were determined using Le Bail's refinement method. The refinement was carried out in the hexagonal space group $P6_{3/m}$.
Fourier transform infrared (FTIR) absorption spectra were recorded using a MIR VERTEX 70 spectrometer (Bruker, Germany) equipped with a monolithic diamond ATR crystal (Quest ATR diamond, Specac, USA). Spectra were recorded over the range of 4000–400 cm^{-1} with a resolution of 2 cm^{-1} and were obtained by averaging the signals obtained from 64 scans. The spectra were normalized with respect to the υ_4 band of the PO_4 group at 600 cm^{-1}, according to a classical procedure [46] relevant for samples with similar B-site compositions. IR band assignment and curve-fitting analysis in the ν_2 (900–840 cm^{-1}) A-type carbonate domain and the ν_3 (1430–1350 cm^{-1}) and ν_2 (890–850 cm^{-1}) B-type carbonate domains were performed using OriginPro 2018b software (OriginLab, U.S.A.) according to a dedicated in-house procedure [47].

The carbonate ion content of each carbonated sample (w/w %) was determined by means of a combustion elemental analyzer (LECO CS-444 carbon/sulfur, LECO Instruments, UK). Measurements were taken in triplicate. The amount of atmospheric CO_2 adsorbed at each powder surface was determined on the corresponding reference sample and then subtracted from the measurements.

2.2.3 Microstructural analysis

The morphological evolution induced by heat treatment under a CO_2-rich atmosphere was observed by scanning electron microscopy (SEM) using a Zeiss Supra 55VP microscope (Carl Zeiss Microscopy GmbH, Oberkochen, Germany) at 1 kV without any coating. Each sample was dispersed by sonication for 5 min in absolute ethanol.

3 Results

3.1 Reference sample characterization

3.1.1 Stoichiometric HA (O_0HA-8.6)

The XRD pattern of O_0HA-8.6 showed a highly crystalline monophasic apatite structure (Figure 1a, in blue). The refined lattice parameters were a = 9.420 Å and c = 6.882 Å (Table 3). Figure 1b displays the IR spectrum of O_0HA-8.6 (in blue) in the ranges 3590–3550 cm^{-1}, 1400–1360 cm^{-1}, 850–810 cm^{-1} and 660–610 cm^{-1}. The IR bands specific to the OH group in the HA environment at 3572 (υ_S) and 628 (υ_L) cm^{-1} were sharp and narrow. No IR band specific to the NO group was observed. SEM images revealed that the O_0HA-8.6 powder was composed of hexagonal prismatic submicrometer-sized crystals (L < 100 nm, Figure 2). The SSA of this powder was determined to be 8.6 $m^2 \cdot g^{-1}$ (Table 3).

Table 3. Thermogravimetric and physicochemical data of the reference samples: mass variation (%) (Eq. 5) recorded during the preparation of the O_xHA samples from O_0HA-8.6 (Figure 3) as well as the A-site composition, lattice parameters (a and c) and SSA of each reference sample

Sample	Mass variation/%	A-site composition	a/Å	c/Å	SSA/m^2 g^{-1}
O_0HA-8.6	n/a	$(OH_{OH})_2$	9.420	6.882	8.6 ± 0.1
$O_{0.4}$HA-5.1	− 0.79	$(OH_{OH})_{1.16}$ $(O'_{OH})_{0.42}$ $(V°_{OH})_{0.42}$	9.418	6.881	5.1 ± 0.1
$O_{0.4}$HA-0.8	− 0.78	$(OH_{OH})_{1.24}$ $(O'_{OH})_{0.38}$ $(V°_{OH})_{0.38}$	9.417	6.883	0.8 ± 0.1
$O_{0.8}$HA-0.8	− 1.43	$(OH_{OH})_{0.42}$ $(O'_{OH})_{0.79}$ $(V°_{OH})_{0.79}$	9.405	6.889	0.8 ± 0.2

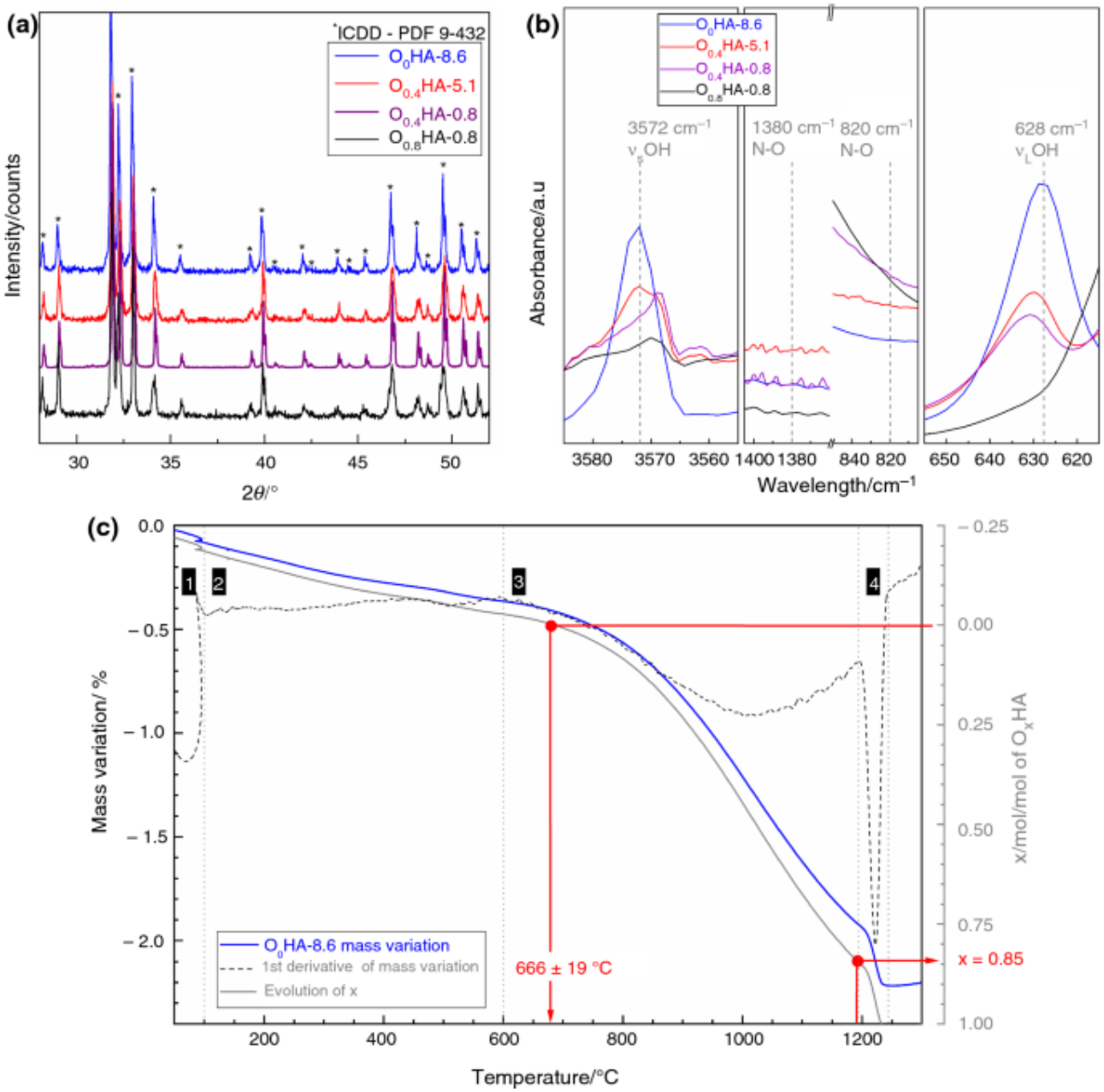

Figure 1. Physicochemical and thermogravimetric analyses of the reference samples. (a) XRD patterns and (b) IR spectra of O_xHA samples, (c) Thermal behavior of O_0HA-8.6 under He flow. The derivative (dotted gray line) of the mass variation (blue line) revealed four domains of temperature. The mass variation (Eq. 4) converted to x content (solid gray line) (see "Manufacture of the reference samples" section) revealed that O_0HA-8.6 dehydration started at 666 ± 19 °C and continued until a critical A-site vacancy of x = 0.85 was reached, where decomposition occurs.

During TGA, O_0HA-8.6 under He was decomposed in four well-known [36, 42, 45, 48] consecutive steps (Figure 1c): RT-100 °C, 100–600 °C, 600–1194 °C and 1194–1300 °C. The first mass loss of 0.08% was attributed to the release of adsorbed species, such as water and CO_2. The second mass loss of 0.29% was attributed to the removal of organic residues (from the synthesis and grinding step) and unbound structural water [44, 49, 50]. The third mass loss of 1.57% was ascribed to the dehydration of the O_0HA-8.6 A-sites (Eq. 2). The last mass loss of 0.28%, above 1194 °C, corresponded to the thermal decomposition of HA into TCP and TTCP according to Eq. (3). A total mass loss of 2.22% was observed.

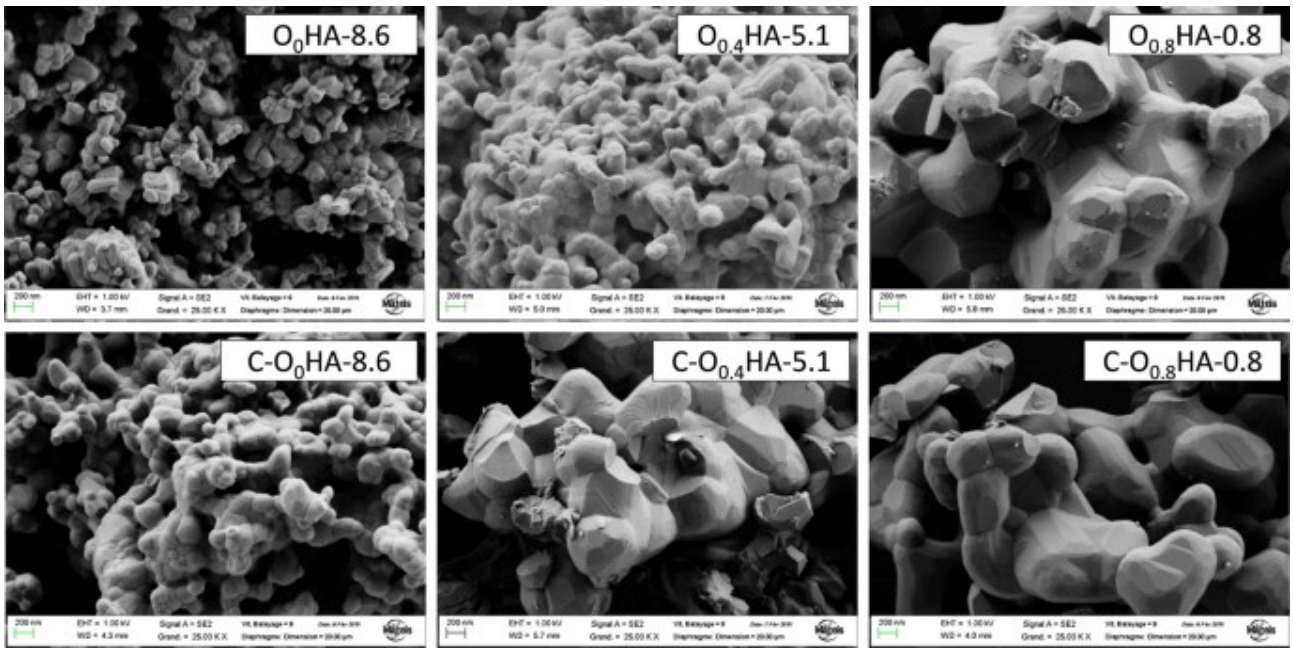

Figure 2. Microstructures of the reference and carbonated samples. SEM micrographs with 25,000× magnification of the O_xHA samples (top) before and (bottom) after heat treatment under a CO2-rich atmosphere for 5 h

3.1.2 O_xHA samples

The O_xHA samples were manufactured with consideration of the thermal stability of O_0HA-8.6 ("Stoichiometric HA (O_0HA-8.6)" section).

Two samples with different A-site compositions, designated hereafter $O_{0.4}$HA-5.1 and $O_{0.8}$HA-0.8, were obtained after heat treatment at 950 °C for 5 h and 1150 °C for 2 h, respectively (Figure 3a, b). As the SSA can modulate the solid–gas exchange reaction, a third O_xHA was designed and manufactured with a chemical composition similar to that of $O_{0.4}$HA-5.1 and an SSA similar to that of $O_{0.8}$HA-0.8. This sample, hereafter designated $O_{0.4}$HA-0.8, was obtained by two-step heat treatment, which consisted of a first isothermal bearing at 1150 °C for 2 h followed by another isothermal bearing at 950 °C for 20 h (Figure 3c).

The TG curve related to the preparation of $O_{0.4}$HA-5.1 showed a significant mass loss during the heating phase and the subsequent isothermal bearing (Figure 3a). This mass variation progressively decreased to a final value of − 0.91%. While the furnace cooled (10 °C·min^{-1}), a 0.12% mass gain was recorded until 500 °C. A change in the mass gain curvature was observed near this temperature, which was selected to fix the composition of $O_{0.4}$HA-5.1 (similar to the procedure used for the other samples). The same patterns were observed in the TG curves of $O_{0.8}$HA-0.8 (Figure 3b) and $O_{0.4}$HA-0.8 (Figure 3c). The mass variations at the end of the last isothermal plateau and at 500 °C during the final cooling were determined to be − 1.56% and 0.13% for $O_{0.8}$HA-0.8 and − 0.88% (from the 12th hour of the plateau to 900 min) and 0.10% for $O_{0.4}$HA-0.8.

At the end of these heat treatments, the SSA was determined to be 5.1 m^2·g^{-1} for the $O_{0.4}$HA-5.1 powder and 0.8 m^2·g^{-1} for both $O_{0.8}$HA-0.8 and $O_{0.4}$HA-0.8 (Table 3).

The X-ray diffraction patterns of O_xHA ($x > 0$) indicated that the samples adopted a highly crystalline monophasic apatite structure (Figure 1a). The lattice parameters a and c of $O_{0.8}$HA-0.8 decreased and increased, respectively, compared to those of O_0HA-8.6, whereas those of $O_{0.4}$HA-5.1 and $O_{0.4}$HA-0.8 remained constant (Table 3).

The IR spectra of O_xHA ($x > 0$) in the ν_S and ν_L OH− and N–O vibration domains are displayed in Figure 1b. IR bands specific to OH groups at 3572 cm^{-1} (υ_S) and 628 cm^{-1} (υ_L) were clearly observed in the $O_{0.4}$HA-5.1 and $O_{0.4}$HA-0.8 spectra but with a lower intensity than those in the O_0HA-8.6 spectrum. On the other hand, both bands were barely noticeable in the $O_{0.8}$HA-0.8 spectrum because of the poor signal-to-noise ratio. No N–O vibration peak, possibly arising from nitrate residues, was observed for any sample.

The $O_{0.4}$HA-5.1 powder consisted of aggregates of faceted ill-shaped crystals of 100 to 300 nm, while the $O_{0.8}$HA-0.8 powder was composed of aggregates of coarse crystals with round facets larger than 400 nm in diameter (Figure 2).

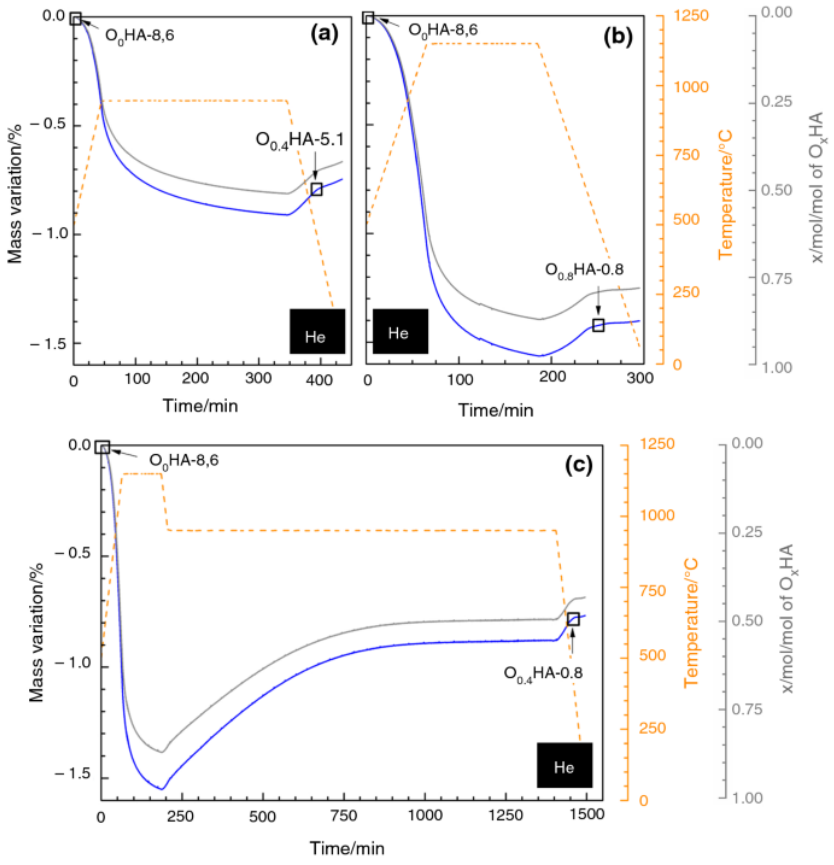

Figure 3. Manufacture of the O_xHA samples. Real-time monitoring of the A-site dehydration x of O_0HA-8.6 by TGA to manufacture (a) $O_{0.4}$HA-5.1, (b) $O_{0.8}$HA-0.8 and (c) $O_{0.4}$HA-0.8. The mass variation signals (blue) (Eq. 5) were converted to x content (solid gray line) (see "Manufacture of the reference samples" section) to reveal the dehydration of the O_0HA-8.6 A-site during the thermal treatment (orange dashed line).

3.2 Heat treatment under a CO_2-rich atmosphere

3.2.1 Real-time monitoring of the exchange reactions with the atmosphere

Figure 4 shows the mass variations of the O_xHA samples heat-treated under a CO_2-rich atmosphere. A mass gain was observed for each sample throughout the heat treatment. When the threshold temperature (950 °C, 30 min < time < 300 min) was reached, the O_0HA-8.6 and $O_{0.4}$HA-5.1 mass gains progressively decreased to constant values of 2.31% and 3.07%, respectively, after approximately 200 min. Under isothermal conditions, the mass gain kinetics of O_0HA-8.6 and $O_{0.4}$HA-5.1 were found to be similar to the exponential law described by Eq. (6), with the parameters listed in Table 4. On the other hand, the mass gains of $O_{0.4}$HA-0.8 and $O_{0.8}$HA-0.8 never plateaued but increased to 2.28% and 3.43%, respectively, at the end of the 950 °C dwell time (Figure 4). These values increased linearly over time from approximately the 150th minute of heat treatment (~ 2 h at isotherm), with rates of increase of 0.003 %·min^{-1} and 0.002 %·min^{-1}, respectively. These mass gain kinetics were described as the sums of two individual exponential laws (Eq. 6), with the k_i and τ_i parameters listed in Table 4.

$$F(t) = A_1\left(1 - e^{-\frac{t}{\tau_1}}\right) + A_2\left(1 - e^{-\frac{t}{\tau_2}}\right) \qquad (6)$$

where F(t) is the mass variation with time at 950 °C, A_i is the pre-exponential factor, τ_i is the characteristic time of the mass variation, and t is the time.

Table 4. Kinetic law constants describing the mass variation of O_xHA samples at 950 °C under a CO2-rich atmosphere, where A_i is the pre-exponential factor and τ_i is the characteristic time of the mass variation expressed by Eq. (6)

Sample	A_1	τ_1/min	A_2	τ_2/min
O_0HA-8.6	1.51	55	0	n/a
$O_{0.4}HA$-5.1	1.47	59	0	n/a
$O_{0.4}HA$-0.8	1.60	266	0.20	24
$O_{0.8}HA$-0.8	1.14	316	0.62	20

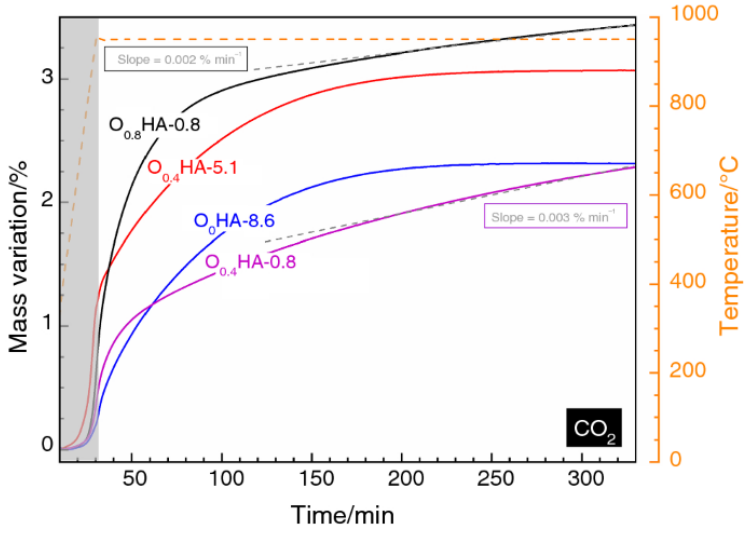

Figure 4. Real-time monitoring of the exchange reactions between the O_xHA samples and a CO_2-rich atmosphere. Mass variations (Eq. 4) of the O_xHA powders throughout heat treatment under a CO_2-rich atmosphere at 950 °C for 5 h (orange dashed line). The gray area shows the time needed to reach the isotherm.

3.2.2 Physicochemical analysis of the carbonated samples

The X-ray diffraction patterns of the carbonated samples indicate a crystalline apatite structure for each sample (Figure 5a). These XRD patterns were consistent with the space group P63/m, and the lattice parameters of each carbonated sample are listed in Table 5. The additional peaks at 30.1° and 35.5° (red arrows) compared to ICDD PDF 009–0432 were attributed to the CHA structure having monoclinic symmetry in space group Pb, equivalent to a double superstructure of hexagonal form [51].

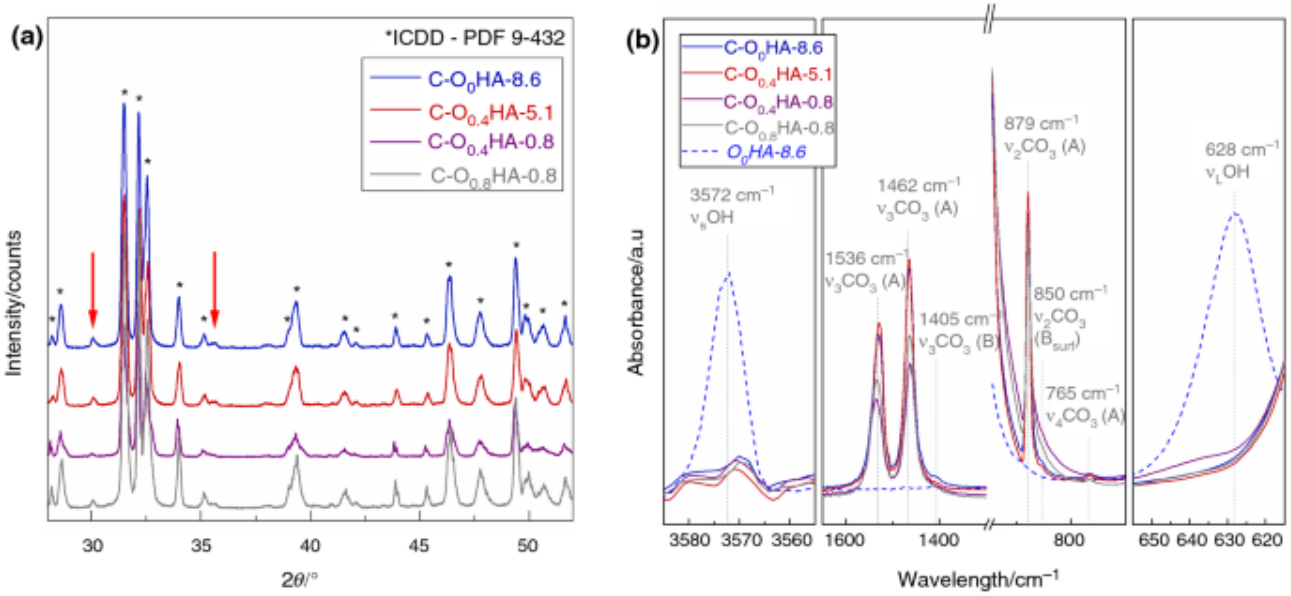

Figure 5. Physicochemical characterization of the carbonated samples. a XRD patterns that revealed extra reflections (red arrows) indicative of monoclinic symmetry (space group Pb) [51] and b IR spectra with, for reference, the O_0HA-8.6 spectrum represented by a blue dotted line.

Table 5. Thermogravimetric and physicochemical data of the carbonated samples

Sample	Mass variation /%	CO_3^{2-} Content /%	A-site composition	a/Å	c/Å	IR band integrated area			SSA/m² g⁻¹
						879 cm−1 A-site CO_3^{2-}	874 cm−1 B- site CO_3^{2-}	1405 cm−1 B- site CO_3^{2-}	
C-O_0HA-8.6	2.31	5.26	$(OH_{OH})_{0.20}$ $(CO_3'_{OH})_{0.90}$ $(V°_{OH})_{0.90}$	9.554	6.865	4.9	0.6	0.06	4.3 ± 0.1
C-$O_{0.4}$HA-5.1	3.07	5.05	$(OH_{OH})_{0.18}$ $(O'_{OH})_{0.05}$ $(CO_3'_{OH})_{0.86}$ $(V°_{OH})_{0.91}$	9.549	6.861	5.3	0.6	0.04	4.2 ± 0.2
C-$O_{0.4}$HA-0.8	2.28	3.74	$(OH_{OH})_{0.66}$ $(O'_{OH})_{0.03}$ $(CO_3'_{OH})_{0.64}$ $(V°_{OH})_{0.67}$	9.530	6.867	3.5	0.6	0	0.8 ± 0.1
C-$O_{0.8}$HA-0.8	3.43	3.51	$(OH_{OH})_{0.62}$ $(O'_{OH})_{0.09}$ $(CO_3'_{OH})_{0.60}$ $(V°_{OH})_{0.69}$	9.539	6.867	4.2	0.6	0	1.1 ± 0.1

Figure 5b displays the IR spectra of C-O_0HA-8.6, C-$O_{0.4}$HA-5.1, C-$O_{0.4}$HA-0.8, and C-$O_{0.8}$HA-0.8 in the υ_S OH− (3585–3555 cm⁻¹), υ_L OH− (655–615 cm⁻¹), υ_3 CO_3^{2-} (1600–1300 cm⁻¹) and υ_2 CO_3^{2-} (900–700 cm⁻¹) domains. IR bands specific to A-type CO_3^{2-} ions in the υ_2 (879 cm⁻¹), υ_3 (*e.g.*, 1536 and 1462 cm⁻¹) and υ_4 (765 cm⁻¹) domains were visible in each IR spectrum. The integrated areas of these bands were determined to be equivalent between C-O_0HA-8.6 and C-$O_{0.4}$HA-5.1 and between C-$O_{0.4}$HA-0.8 and C-$O_{0.8}$HA-0.8 (see the integrated area of the band at 879 cm⁻¹ in Table 5). Absorption bands with very low intensities assigned to B-type CO_3^{2-}ions were also detected, at 1405 cm⁻¹ (υ_3) and 874 cm⁻¹ (υ_2). The integrated area ratio of $I_{\nu_2}^{CO_3^B}(874)/I_{\nu_2}^{CO_3^A}(879)$ remained relatively low and constant for all samples (ranging between 0.1 and 0.2, Table 5), while a low-intensity band of υ_3 CO_3- B (1405 cm⁻¹) was observed only for samples C-O_0HA-8.6 and C-$O_{0.4}$HA-5.1 (Figure 5b). IR bands attributed to OH groups at 3572 cm⁻¹ (υ_S) and 628 cm⁻¹ (υ_L) were not observed or were observed to have a very low intensity (υ_L OH of C-$O_{0.4}$HA-0.8 sample) in all carbonated sample spectra because of the poor signal-to-noise ratio.

The carbonate ion content (w/w %) was determined to be 5.26 ± 0.04%, 5.05 ± 0.09%, 3.74 ± 0.05% and 3.51 ± 0.06% for C-O_0HA-8.6, C-$O_{0.4}$HA-5.1, C-$O_{0.4}$HA-0.8, and C-$O_{0.8}$HA-0.8, respectively (Table 5).

3.2.3 Microstructural evolutions

Heat treatment under a CO_2-rich atmosphere induced coalescence and slight but normal grain growth for O_0HA-8.6, accompanied by a 50% reduction in the SSA (Figure 2 and Table 3 *vs.* Table 5). More substantial normal grain growth and an 18% reduction in the SSA were observed for $O_{0.4}$HA-5.1. In contrast, neither morphological changes nor a surface area reduction were observed for $O_{0.8}$HA-0.8.

4 Discussion

4.1 Manufacture of the reference samples

This section discusses the thermogravimetric analysis of O_0HA-8.6 under He and explains how the results were exploited to manufacture the reference O_xHA powders with adjusted and complementary A-site compositions and SSAs required to understand the solid–gas exchange reactions under a CO_2-rich atmosphere.

The onset of A-site dehydration in O_0HA-8.6 in Figure 1c was not discernible because of a concomitant loss of organic residues from the powder (resulting from grinding). To overcome this issue, the relative mass variation ($\Delta m''/m_{1300}$), Eq. (7), determined from Figure 1c, was calculated to determine the stoichiometric coefficient x per mole of O_xHA according to Eq. (8).

$$\frac{\Delta m''}{m_{1300}} = \frac{m_T - m_{1300}}{m_{1300}} = \frac{(n_{OxHA}M_{OxHA}) - (n_{TCP}M_{TCP} + n_{TTCP}M_{TTCP})}{n_{TCP}M_{TCP} + n_{TTCP}M_{TTCP}} \quad (7)$$

$$x = 1 - \frac{\Delta m''}{m_{1300}} \times \frac{2M_{TCP} + M_{TTCP}}{M_{H_2O}} \quad (8)$$

where m_T and m_{1300} and are the sample mass at T and 1300 °C, respectively, and n_i and M_i are the amount and molar mass of compound i. Under our experimental conditions, the decomposition of O_xHA (Eq. 3) was assumed to be complete at 1300 °C.
The evolution of x with temperature is plotted in gray in Figure 1c. The results indicate that under these dynamic conditions, A-site dehydration of O_0HA-8.6 began at 666 ± 19 °C, and decomposition occurred at 1194 °C for x = 0.85 (i.e., an A-site composition of $(OH)_{0.30}O_{0.85}(VOH)_{0.85}$). The mass loss recorded between room temperature and 666 °C was attributed to the removal of organic residues.
For subsequent experiments, the thermal treatment applied during the manufacture of the reference samples was performed at temperatures below the O_0HA-8.6 decomposition temperature, and residues were removed from the starting powder O_0HA-8.6 by a preliminary 5 h isothermal bearing at 500 °C (data not shown). Thus, the mass variations recorded during the thermal treatments applied during the preparation of the reference $O_{0.4}HA$-5.1, $O_{0.4}HA$-0.8, and $O_{0.8}HA$-0.8 samples and displayed in Figure 3 correspond to the A-site composition changes described by Eq. (2): a mass loss corresponding to A-site dehydration and a mass gain corresponding to A-site rehydration. The relative mass variation (Eq. 9) displayed in Figure 3 was used to determine the stoichiometric coefficient x per mole of O_xHA according to Eq. (10). A transformed curve in x content was then proposed for each sample (gray patterns in Figure 3).

$$\frac{\Delta m'}{m_{500}} = \frac{m_T - m_{500}}{m_{500}} = \frac{(n_{OxHA}M_{OxHA}) - (n_{HA}M_{HA})}{n_{HA}M_{HA}} \quad (9)$$

$$x = -\frac{\Delta m'}{m_{500}} \times \frac{M_{HA}}{M_{H_2O}} \quad (10)$$

where m_T and m_{500} are the sample mass at T and after isotherm bearing at 500 °C for 5 h, respectively, and n_i and M_i are the amount and molar mass of compound i, respectively.
The A-site compositions of $O_{0.4}HA$-5.1, $O_{0.4}HA$-0.8, and $O_{0.8}HA$-0.8 were determined at the curvature change point during the cooling step (~ 500 °C, black box, Figure 3) according to Eq. (10) and were expressed by formula in Eqs. (11), (12) and (13), respectively.

$$(OH_{OH})_{1.16\pm0.06}(O'_{OH})_{0.42\pm0.03}(V^o_{OH})_{0.42\pm0.03} \quad (\textit{i.e. } O_xHA \text{ with x=0.42}) \quad (11)$$

$$(OH_{OH})_{1.06\pm0.1}(O'_{OH})_{0.47\pm0.05}(V^o_{OH})_{0.47\pm0.05} \quad (\textit{i.e. } O_xHA \text{ with x=0.47}) \quad (12)$$

$$(OH_{OH})_{0.42\pm0.12}(O'_{OH})_{0.79\pm0.06}(V^o_{OH})_{0.79\pm0.06} \quad (\textit{i.e. } O_xHA \text{ with x=0.79}) \quad (13)$$

$O_{0.4}HA$-5.1 and $O_{0.4}HA$-0.8 were found to have equivalent A-site compositions.
As a result, four crystalline monophasic O_xHA with three different A-site compositions and three different SSAs were successfully produced based on controlled chemical synthesis and thermal treatments (Figure 1a, Table 3), enabling the evaluation of the influence of both parameters on the exchange reactions between the apatite structure and the heat treatment atmosphere.

4.2 Qualitative analysis of the solid–gas exchange reactions

This section explains the particular roles of both the A-site composition and the SSA parameters on A- and B-type carbonate substitution in O_xHA upon heat treatment under a CO_2-rich atmosphere, as well as the difference between the TG data and the quantification of the carbonate content after heat treatment under a CO_2-rich atmosphere.
Heat treatment of the four reference samples under a CO_2-rich atmosphere effectively induced substitution of CO_3^{2-} ions for OH^- ions, as shown by the carbon titration and the evolution of the lattice parameters (Table 5) with respect to literature data [19, 52]. However, trace B-type CO_3^{2-} ions were indicated in the IR spectra (Figure 5b). Although this result was unexpected, since B-type CO_3^{2-} ions are mostly inserted in the apatite lattice through low-temperature aqueous precipitation [24, 25, 53], the substitution of CO_3^{2-} ions for PO43− ions has previously been observed after sintering HA at 1300 °C under CO_2 [54] and can be attributed to the absorption of CO_3^{2-} at the surface of the crystals. Considering the very low intensity of these IR bands, the B-type CO_3^{2-} ions were ignored in the following discussion.
Heat treatment at 950 °C for 5 h in a CO_2-rich atmosphere induced significant mass gains of 2.31%, 3.07%, 2.28% and 3.43% for O_0HA-8.6, $O_{0.4}HA$-5.1, $O_{0.4}HA$-0.8 and $O_{0.8}HA$-0.8, respectively (Figure 4).

These mass gains could not be attributed to the substitution of CO_3^{2-} ions for OH− ions only, as an equivalent carbonate content was measured for C-O_0HA-8.6 and C-$O_{0.4}$HA-5.1 (approximately 5%, Table 5) and for C-$O_{0.4}$HA-0.8 and C-$O_{0.8}$HA-0.8 (approximately 3.5%). This apparent conflict in the results could be explained by the co-occurrence of two different reactions during heat treatment under the CO_2-rich atmosphere: A-site CO_3^{2-} ion substitution and A-site dehydration. Indeed, A-site dehydration and enrichment in CO_3^{2-} ions induced opposite mass changes. To compare the extent of exchange reactions (EER) in A-sites during the heat treatment of powders under a CO_2-rich atmosphere, the ratios (Eq. 14) of the mass variation (Figure 4) to the theoretical value that would be reached for stoichiometric A-type carbonate apatite (C_AHA, $Ca_{10}(PO_4)_6(CO_3)$, [19]) were plotted (Figure 6).

$$EER = \frac{Mass\ variation\ (\%)}{\frac{m_{C_AHA} - m_{O_xHA}}{m_{O_xHA}}} = \frac{M(t) - M_{O_xHA}}{M_{C_AHA} - M_{O_xHA}} \qquad (14)$$

where M_i represents the molar mass of compound i and M(t) is the molar mass of the powder at time t during thermal treatment under a CO_2-rich atmosphere.

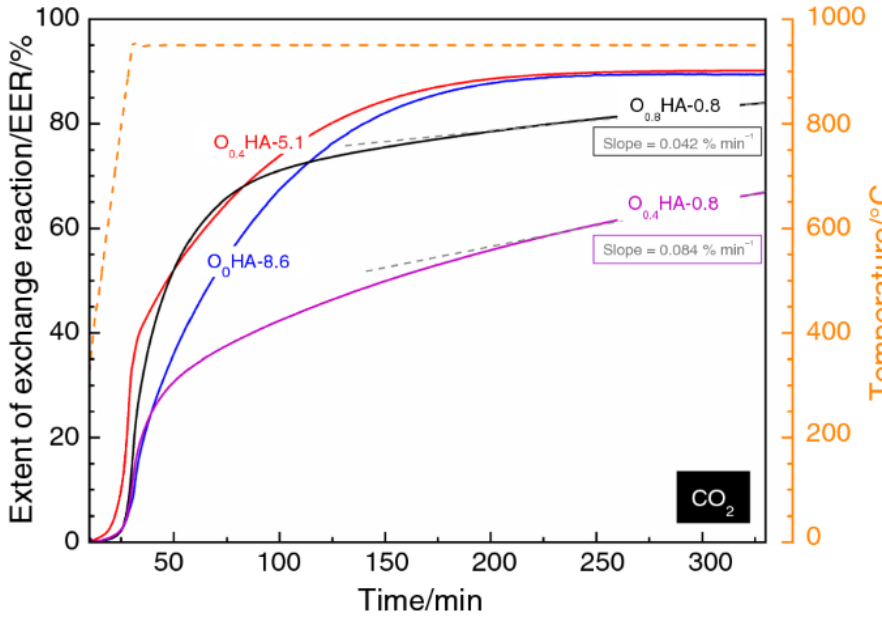

Figure 6. EER in the A-site of O_xHA throughout heat treatment under a CO_2-rich atmosphere. The mass variations (Figure 4) have been converted into EER during heat treatment (orange dotted line) according to Eq. (14).

The shape of the TG curves (Figure 4) was preserved through mathematical transformation (Figure 6). The EER at the A-site for both O_0HA-8.6 and $O_{0.4}$HA-5.1 reached equilibrium with equivalent final values (89.1 ± 0.8% and 87.6 ± 1.7%, respectively). No plateau was achieved for either $O_{0.4}$HA-0.8 or $O_{0.8}$HA-0.8. The curves were well fitted with linear increasing functions: 0.08% min−1 and 0.04% min−1. After 5 h at 950 °C, the EER was 64.3 ± 4.5% and 78.3 ± 5.6% for $O_{0.4}$HA-0.8 and $O_{0.8}$HA-0.8, respectively. These results were consistent with the carbon titration results (Table 5); $O_{0.4}$HA-0.8 (3.5% w/w) contained less carbon than $O_{0.8}$HA-0.8 (3.8% w/w) and less carbon than both O_0HA-8.6 and $O_{0.4}$HA-5.1 (5% w/w). The SSA, rather than the composition of the A sites, explains the difference in the solid–gas exchange kinetics between O_0HA-8.6/ $O_{0.4}$HA-5.1 and $O_{0.4}$HA-0.8/ $O_{0.8}$HA-0.8: $O_{0.4}$HA-5.1 and $O_{0.4}$HA-0.8 exhibited the same composition but different exchange kinetics (Table 4), unlike $O_{0.4}$HA-0.8 and $O_{0.8}$HA-0.8. In other words, thermal enrichment of the CO_3^{2-} ions in the A-sites under a CO_2-rich atmosphere is a standard surface-driven mechanism.

Moreover, densification and grain growth (Figure 2), resulting in decreases in the SSAs of O_0HA-8.6 and $O_{0.4}$HA-5.1 upon heat treatment at 950 °C for 5 h under a CO_2-rich atmosphere (Table 3 *vs.* Table 5), explain the trace B-type CO_3^{2-} ions observed in C-O_0HA-8.6 and C-$O_{0.4}$HA-5.1 (Figure 7, appendix): CO2 adsorbed at the crystallite surface was embedded in the B-site at the grain surface or boundary. Reciprocally, A-site CO32− ion substitution further decreased the SSA: C-O_0HA-8.6 had a lower SSA (4.3 $m^2 \cdot g^{-1}$) than $O_{0.4}$HA-5.1 (5.1 $m^2 \cdot g^{-1}$) despite having a similar thermal history (950 °C for 5 h either under a CO_2-rich atmosphere for C-O_0HA-8.6 or under a He-rich atmosphere for $O_{0.4}$HA-5.1). This phenomenon has been reported previously [54], but no explanation was ever proposed. The generation

of a large amount of A-site vacancies throughout calcination under a CO_2-rich atmosphere (0.90 mol of vacancies per mol of C-O_0HA-8.6 compared to 0.42 mol of vacancies per mol of $O_{0.4}$HA-5.1; see "A-site composition after heat treatment under a CO_2-rich atmosphere and associated exchange reactions" section, Table 3 and Table 5) may favor matter diffusion.

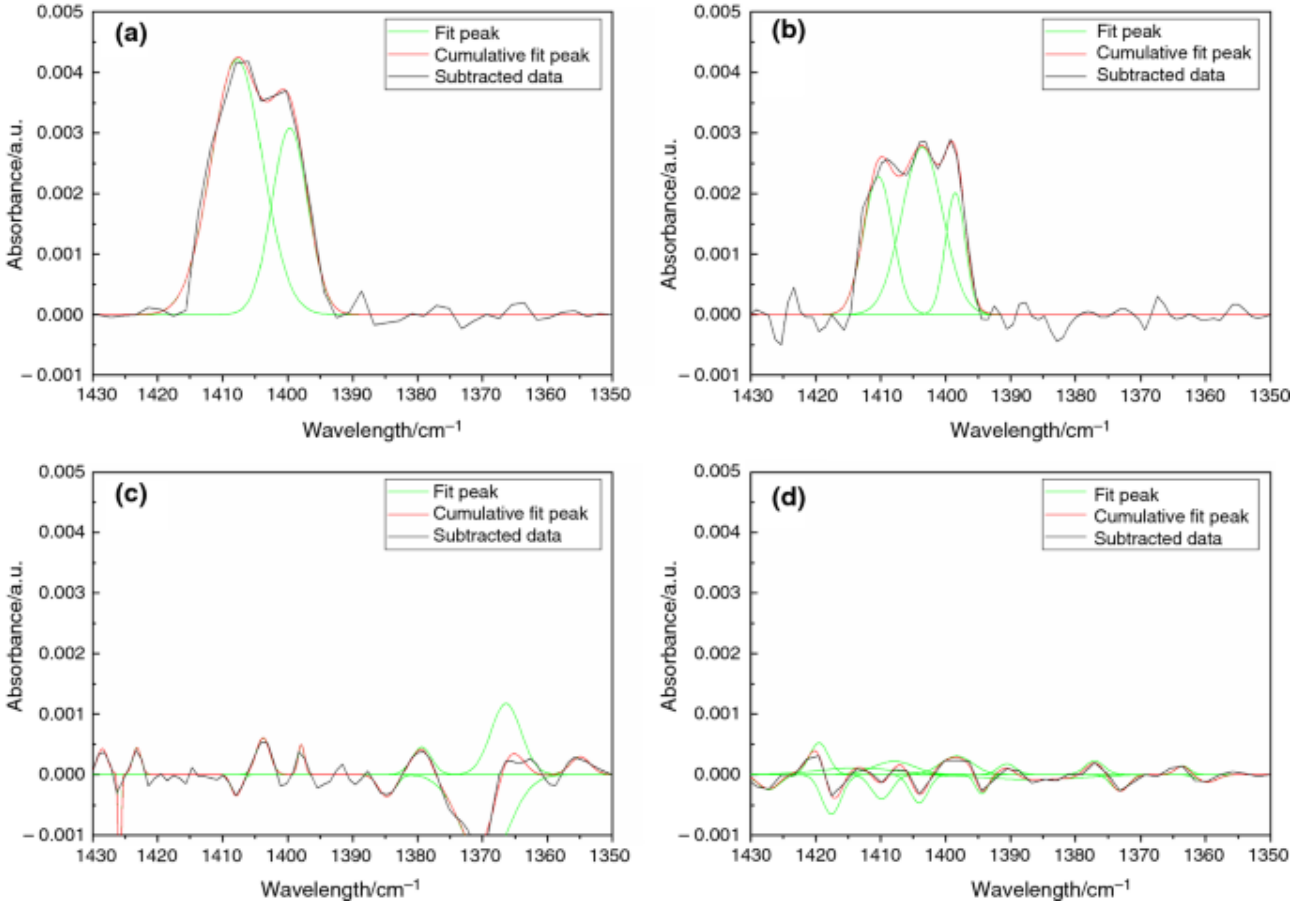

Figure 7 . Appendix: curve-fitting results in the ν3 (1430–1350 cm⁻¹) B-type carbonate domain of carbonated samples: a C-O_0HA-8.6, b C-$O_{0.4}$HA-5.1, c C-$O_{0.4}$HA-0.8 and d C-$O_{0.8}$HA-0.8

4.3 A-site composition after heat treatment under a CO_2-rich atmosphere and associated exchange reactions

This final section aims to establish the mass balance equations corresponding to the exchange reactions between O_xHA and the CO_2-rich atmosphere at a high temperature (950 °C) and to discuss the key influence of the initial A-site composition.

As the amount of CO3 in the B-sites is insignificant, the composition of the samples heat-treated under a CO_2-rich atmosphere corresponds to carbonated oxy-hydroxyapatite (CaOyHA) with the following general formula (Eq. 15):

$$Ca_{10}(PO_4)_6(OH)_{2-2y-2a}O_y(CO_3)_a \qquad (15)$$

The stoichiometric coefficients a and y were determined through the quantification of the CO_3^{2-} content of CaOyHA and the mass variation recorded during the heat treatment of the reference samples under a CO_2-rich atmosphere (Figure 4). Therefore, coefficient a for each CaOyHA can be determined by Eq. (16):

$$a = carbonate\ content\ (\%) \times \frac{M_{Ca_aO_yHA}}{100\ M_{CO_3}} \qquad (16)$$

In the context of this study, A-site vacancies (V°OH) were formed by the concomitant incorporation of CO_3^{2-} ions in the A-site (Eq. 1) and the partial dehydration of CaOyHA (Eq. 2) according to the general equilibrium described by Eq. (17):

$$Ca_{10}(PO_4)_6(OH)_{2-2x}O_x + aCO_2 \leftrightarrow Ca_{10}(PO_4)_6(OH)_{2-2y-2a}O_y(CO_3)_a + (y+a)H_2O \quad (17)$$

with x determined in "Manufacture of the reference samples" section and a determined from Eq. (16). The coefficient y can be determined from the mass variation (%) of O_xHA during heat treatment according to Eqs. (18) and (19):

$$Mass\ variation\ (\%) = \frac{M_{Ca_OyHA} - M_{OxHA}}{M_{O_xHA}} = \frac{aM_{CO_2} + (x-y-a)M_{H_2O}}{M_{O_xHA}} \quad (18)$$

$$y = \frac{(x-a)M_{H_2O} - (a)M_{CO_2} - (Mass\ variation(\%)) \times M_{O_xHA}}{M_{H_2O}} \quad (19)$$

Therefore, by using the TG and carbonate content data compiled in Table 5, the A-site composition of C-O_0HA-8.6 (Eq. 20), C-$O_{0.4}$HA-5.1 (Eq. 21), C-$O_{0.4}$HA-0.8 (Eq. 22) and C-$O_{0.8}$HA-0.8 (Eq. 23) can be written as follows:

$$(OH_{OH})_{0.2\pm0.03}\left(CO'_{3\,OH}\right)_{0.90\pm0.01}(V^o_{OH})_{0.90\pm0.02}$$
(*i.e.* C_aO_yHA with y=0 and a=0.90) (20)

$$(OH_{OH})_{0.18\pm0.06}(O'_{OH})_{0.05\pm0.03}\left(CO'_{3\,OH}\right)_{0.80\pm0.03}(V^o_{OH})_{0.91\pm0.06}$$
(*i.e.* C_aO_yHA with y=0.05 and a=0.86) (21)

$$(OH_{OH})_{0.66\pm0.04}(O'_{OH})_{0.03\pm0.01}\left(CO'_{3\,OH}\right)_{0.04\pm0.02}(V^o_{OH})_{0.67\pm0.02}$$
(*i.e.* C_aO_yHA with y=0.03 and a=0.67) (22)

$$(OH_{OH})_{0.62\pm0.06}(O'_{OH})_{0.09\pm0.03}\left(CO'_{3\,OH}\right)_{0.60\pm0.03}(V^o_{OH})_{0.69\pm0.06}$$
(*i.e.* C_aO_yHA with y=0.09 and a=0.60) (23)

OH^- ions were present in the A-sites of all carbonated samples, contrary to the prediction based on the absence of IR bands specific to OH groups in the HA environment at 3572 (ν_S) and 628 (ν_L) cm^{-1} (Figure 5b). The absence of this IR band in C_aO_yHA spectra has previously been observed and attributed to hindered librational movement of the OH^- ions as a result of substitutions with A-type CO_3^{2-} ions, from 0.2 A-type CO_3^{2-} ion [19]. Moreover, the high A-site vacancy content (0.9, Eqs. (20) and (21)) evaluated in C-O_0HA-8.6 and C-$O_{0.4}$HA-5.1, which was higher than the critical A-site vacancy content determined for O_0HA-8.6 ("Manufacture of the reference samples" section: $(OH)_{0.30}O_{0.85}(VOH)_{0.85}$), confirmed that the substitution of CO_3^{2-} for OH− stabilized the apatite structure [55, 56] while allowing two space groups. Furthermore, the constant EER value discussed previously (Figure 6) and the equivalent A-site composition in C-O_0HA-8.6 and C-$O_{0.4}$HA-5.1 (Eqs. 20 and 21) ≈ $(OH)_{0.19\pm0.05}$ $O_{0.03\pm0.02}$ $(CO3)_{0.88\pm0.02}$) upon heat treatment at 950 °C for 5 h under a CO_2-rich atmosphere (p_{CO2} = 101.28 kPa and p_{H2O} = 0.02 kPa), proves that thermodynamic equilibrium was achieved for these samples. Conversely, C-$O_{0.4}$HA-0.8 and C-$O_{0.8}$HA-0.8 were still undergoing exchange reactions with the atmosphere after 5 h at 950 °C. In addition, while the quantities of OH^x_{OH}decreased for samples O_0HA-8.6, $O_{0.4}$HA-5.1, and $O_{0.4}$HA-0.8 during heat treatment under a CO_2-rich atmosphere (formula in Table 3 *vs.* in Table 5), that of $O_{0.8}$HA-0.8 increased (0.42 to 0.62), indicating that, for the specific composition of $O_{0.8}$HA-0.8, incorporation of carbonate in A-sites was accompanied by rehydration.

Despite the low H_2O partial pressure in the heat treatment atmosphere (0.02 kPa), this rehydration was indeed possible. Figure 8 shows the mass variation of $O_{0.4}$HA-5.1, $O_{0.4}$HA-0.8, and $O_{0.8}$HA-0.8 upon heat treatment at 950 °C for 5 h under He containing 0.02 kPa of H2O. At the end of this thermal treatment, $O_{0.4}$HA-5.1 and $O_{0.4}$HA-0.8 exhibited mass losses of 0.43% and 0.30%, respectively, whereas $O_{0.8}$HA-0.8 exhibited a mass gain of 0.26%. These mass variations correspond to an A-site dehydration of 0.64 and 0.57 mol of H_2O per mol of apatite and a rehydration of 0.66 mol of H2O per mol of apatite, respectively (from Eqs. (17) and (19) with a = 0).

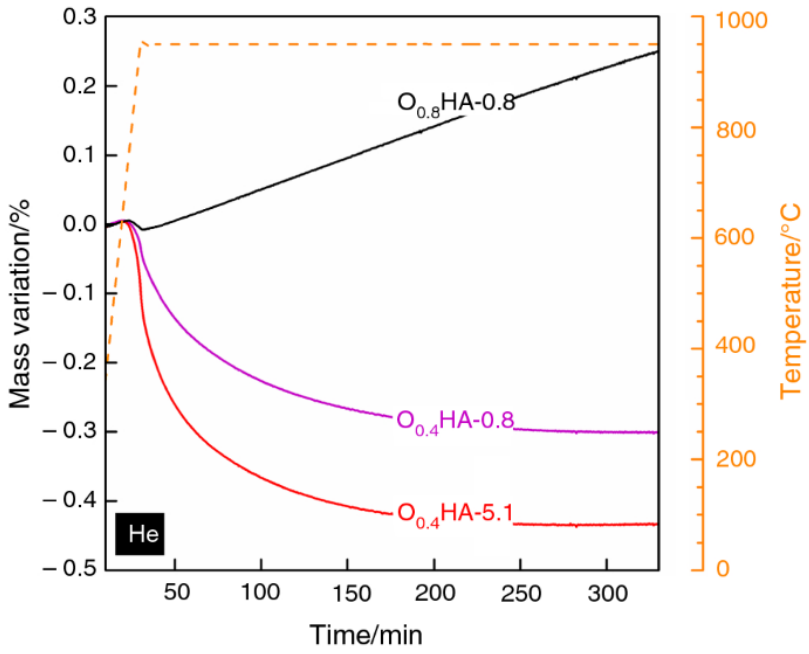

Figure 8. Dehydration or rehydration of O_xHA samples with temperature with respect to the A-site composition. Mass variation of $O_{0.4}$HA-5.1 (red line), $O_{0.4}$HA-0.8 (purple line), and $O_{0.8}$HA-0.8 (black line) samples heat-treated under He at 950 °C for 5 h (orange dashed line).

The corresponding mass balance of O_0HA-8.6, $O_{0.4}$HA-5.1, $O_{0.4}$HA-0.8 and $O_{0.8}$HA-0.8 heat-treated under a CO_2-rich atmosphere can be written as follows (Eqs. (24), (25), (26) and (27), respectively).

$$(O_0HA - 8.6) + 0.90\ CO_2^{(g)} \rightarrow (C - O_0HA - 8.6) + 0.90\ H_2O^{(g)} \quad (24)$$

$$(O_{0.4}HA - 5.1) + 0.86\ CO_2^{(g)} \rightarrow (C - O_{0.4}HA - 5.1) + 0.49\ H_2O^{(g)} \quad (25)$$

$$(O_{0.4}HA - 0.8) + 0.67\ CO_2^{(g)} \rightarrow (C - O_{0.4}HA - 0.8) + 0.2\ H_2O^{(g)} \quad (26)$$

$$(O_{0.8}HA - 0.8) + 0.60\ CO_2^{(g)} + 0.10\ H_2O^{(g)} \rightarrow (C - O_{0.4}HA - 0.8) \quad (27)$$

The mass balance between O_0HA-8.6 and C-O_0HA-8.6 (Eq. 24) is simple, as shown in Eq. (1), while a linear combination of Eqs. (1) and (2) is necessary for $O_{0.4}$HA-5.1, $O_{0.4}$HA-0.8 and $O_{0.8}$HA-0.8, as shown by Eqs. (28), (29) and (30), respectively.

$$\begin{cases} 0.86\left[CO_2^{(g)} + 2\ OH_{OH}^X \rightarrow CO_3'_{OH} + V_{OH}^o + H_2O^{(g)}\right] \\ 0.37\left[O'_{OH} + V_{OH}^o + H_2O^{(g)} \rightarrow 2\ OH_{OH}^X\right] \end{cases} \quad (28)$$

$$\begin{cases} 0.67\left[CO_2^{(g)} + 2\ OH_{OH}^X \rightarrow CO_3'_{OH} + V_{OH}^o + H_2O^{(g)}\right] \\ 0.47\left[O'_{OH} + V_{OH}^o + H_2O^{(g)} \rightarrow 2\ OH_{OH}^X\right] \end{cases} \quad (29)$$

$$\begin{cases} 0.60\left[CO_2^{(g)} + 2\ OH_{OH}^X \rightarrow CO_3'_{OH} + V_{OH}^o + H_2O^{(g)}\right] \\ 0.70\left[O'_{OH} + V_{OH}^o + H_2O^{(g)} \rightarrow 2\ OH_{OH}^X\right] \end{cases} \quad (30)$$

Considering the very low H_2O partial pressure (0.02 kPa) and the fact that 1.2 OH_{OH}^X (0.60 × 2) are necessary in Eq. (30) to incorporate 0.6 CO_3^{2-} ion in the A-site (i.e., 0.62 to obtain the final A-site composition provided in Table 5), although only 0.42 OH_{OH}^X are initially available (Table 3: $(OH_{OH})_{0.42}(O'_{OH})_{0.79}(V°_{OH})_{0.79}$), another set of elementary reactions can be considered to better fit the experimental results. Indeed, assuming that the substitution of CO_3^{2-} ions for OH− ions could result from a reaction between CO_2 and A-site oxygen ions (Eq. 31), a linear combination of both Eq. (31) and Eq. (2) can suitably describe the exchange reactions (Eqs. 25 to 27), as shown by Eqs. (32)–(34).

$$CO_2^{(g)} + O'_{OH} \rightarrow CO_3{}'_{OH} \quad (31)$$

$$\begin{cases} 0.86\left[CO_2^{(g)} + O'_{OH} \rightarrow CO_3{}'_{OH}\right] \\ 0.49\left[2\,OH_{OH}^{X} \rightarrow O'_{OH} + V_{OH}^{o} + H_2O^{(g)}\right] \end{cases} \quad (32)$$

$$\begin{cases} 0.66\left[CO_2^{(g)} + O'_{OH} \rightarrow CO_3{}'_{OH}\right] \\ 0.20\left[2\,OH_{OH}^{X} \rightarrow O'_{OH} + V_{OH}^{o} + H_2O^{(g)}\right] \end{cases} \quad (33)$$

$$\begin{cases} 0.60\left[CO_2^{(g)} + O'_{OH} \rightarrow CO_3{}'_{OH}\right] \\ 0.10\left[O'_{OH} + V_{OH}^{o} + H_2O^{(g)} \rightarrow 2\,OH_{OH}^{X}\right] \end{cases} \quad (34)$$

Thus, depending on the initial A-site composition, two mechanisms driving exchange reactions between CO2 gas and the A-sites can occur. If the initial A-site oxygen content in O_xHA is below 0.42 ($O_{0.4}$HA-5.1 and $O_{0.4}$HA-0.8, Table 3), A-site dehydration occurs, plausibly creating reactive sites for the incorporation of CO_3^{2-} ions in the A-sites. If the initial A-site oxygen content is greater than or equal to 0.79 ($O_{0.8}$HA-0.8), A-site rehydration takes place and competes with A-site CO_3^{2-} ion substitution to consume A-site oxygen ions.

These results prove that the preparation of O_xHA powders (i.e., thermal pretreatment) plays a key role in the high-temperature exchange reactions between a CO_2-rich atmosphere and the A-site. The partial pressures of CO_2 and H_2O jointly contribute to the solid–gas exchange reactions, despite the very low H_2O partial pressure (0.02 kPa).

Conclusions

Controlled A-site dehydration through heat treatment under He was used to tune the initial A-site composition and SSA of a monophasic and stoichiometric HA powder. The resulting A-site composition of oxy-hydroxyapatite (O_xHA) samples significantly influenced the thermal exchange reactions between the apatite structure and the CO_2-rich atmosphere; the occurrence of A-site dehydration or hydration depended on the initial O'_{OH} (or V_{OH}^{o}) concentration in the A-site. Moreover, even under a very low partial pressure of H_2O (0.02 kPa), water vapor can contribute to the solid–gas exchange reaction and can compete with atmospheric CO_2 (and the associated A-site CO_3^{2-} ion substitution). When O_xHA initially contained a critically high number of OH vacancies (V_{OH}^{o}), the A-type carbonate ion substitution mechanism could more accurately be described by $CO_2^{(g)} + O'_{OH} \rightarrow CO_3{}'_{OH}$ than by the standard $CO_2^{(g)} + 2\,OH_{OH}^{X} \rightarrow CO_3{}'_{OH} + V_{OH}^{o} + H_2O^{(g)}$.

Thermal enrichment of the A-sites with CO_3^{2-} ions under a CO_2-rich atmosphere occurred by a standard surface-driven mechanism modulated by the A-site composition of O_xHA. As a result, thermal pretreatment of HA powder prior to sintering cannot be regarded as a trivial step. This treatment must be carefully chosen to obtain a powder whose physicochemical characteristics and thermal behavior will enable obtaining a bioceramic with the desired properties.

Acknowledgements
We acknowledge Coralie Laurent from Mines Saint Etienne and Philipe Steyer and Annie Malchère from INSA Lyon for technical help.

Funding
This study was funded by the Auvergne-Rhone Alpes region (ARC2 program, PhD fellowship to SG).
Author information

Contributions
All authors contributed to the study conception and design. Material preparation, data collection and analysis were performed by SG, ND and DM. The first draft of the manuscript was written by SG and DM, and all authors commented on previous versions of the manuscript. All authors read and approved the final manuscript.

Conflict of interest
The authors have no competing interests to declare that are relevant to the content of this article.

References
1. Campana V, Milano G, Pagano E, Barba M, Cicione C, Salonna G, et al. Bone substitutes in orthopaedic surgery: from basic science to clinical practice. J Mater Sci-Mater M. 2014;25(10):2445–61. https://doi-org/10.1007/s10856-014-5240-2
2. Marchat D, Champion E. Chapter 8: ceramic devices for bone replacement: mechanical and clinical issues. In: Palmero P, Barra ED, Cambier F, editors. Advances in ceramic biomaterials medical and commercial requirements. Woodhead publishing, Elsevier; 2017. p. 279–311. https://doi-org/10.1016/B978-0-08-100881-2.00008-7.
3. Porter A, Patel N, Brooks R, Best S, Rushton N, Bonfield W. Effect of carbonate substitution on the ultrastructural characteristics of hydroxyapatite implants. J Mater Sci Mater Med. 2005;16(10):899–907. https://doi-org/10.1007/s10856-005-4424-1.
4. Spence G, Patel N, Brooks R, Bonfield W, Rushton N. Osteoclastogenesis on hydroxyapatite ceramics: the effect of carbonate substitution. J Biomed Mater Res A. 2010;92(4):1292–300. https://doi-org/10.1002/jbm.a.32373.
5. Barralet J, Akao M, Aoki H, Aoki H. Dissolution of dense carbonate apatite subcutaneously implanted in Wistar rats. J Biomed Mater Res. 2000;49(2):176–82. https://doi-org/10.1002/(sici)1097-4636(200002)49:2%3C176::aid-jbm4%3E3.0.co;2-8.
6. Detsch R, Mayr H, Ziegler G. Formation of osteoclast-like cells on HA and TCP ceramics. Acta Biomater. 2008;4(1):139–48. https://doi-org/10.1016/j.actbio.2007.03.014.
7. Calori GM, Mazza E, Colombo M, Ripamonti C. The use of bone-graft substitutes in large bone defects: Any specific needs? Injury. 2011;42:S56–63. https://doi-org/10.1016/j.injury.2011.06.011.
8. Collins KL, Gates EM, Gilchrist CL, Hoffman BD. Chapter 1: bio-instructive cues in scaffolds for musculoskeletal tissue engineering and regenerative medicine. In: Brown JL, Kumbar SG, Banik BL, editors. Bio-instructive scaffolds for musculoskeletal tissue engineering and regenerative medicine. Academic Press; 2017. p. 3–35. https://doi-org/10.1016/B978-0-12-803394-4.00001-X.
9. Rey C, Combes C, Drouet C, Glimcher MJ. Bone mineral: update on chemical composition and structure. Osteoporosis Int. 2009;20(6):1013–21. https://doi-org/10.1007/s00198-009-0860-y.
10. Cazalbou S, Combes C, Eichert D, Rey C. Adaptative physico-chemistry of bio-related calcium phosphates. J Mater Chem. 2004;14(14):2148–53. https://doi-org/10.1039/B401318B.
11. Melville AJ, Harrison J, Gross KA, Forsythe JS, Trounson AO, Mollard R. Mouse embryonic stem cell colonisation of carbonated apatite surfaces. Biomaterials. 2006;27(4):615–22. https://doi-org/10.1016/j.biomaterials.2005.06.028.
12. Habraken W, Habibovic P, Epple M, Bohner M. Calcium phosphates in biomedical applications: Materials for the future? Mater Today. 2016;19(2):69–87. https://doi-org/10.1016/j.mattod.2015.10.008.

13. Paré A, Charbonnier B, Tournier P, Vignes C, Veziers J, Lesoeur J, et al. Tailored three-dimensionally printed triply periodic calcium phosphate implants: a preclinical study for craniofacial bone repair. ACS Biomater Sci Eng. 2020;6(1):553–63. https://doi-org/10.1021/acsbiomaterials.9b01241.
14. Barrere F, van Blitterswijk CA, de Groot K. Bone regeneration: molecular and cellular interactions with calcium phosphate ceramics. Int J Nanomed. 2006;1(3):317–32.
15. Spence G, Phillips S, Campion C, Brooks R, Rushton N. Bone formation in a carbonate-substituted hydroxyapatite implant is inhibited by zoledronate: the importance of bioresorption to osteoconduction. J Bone Joint Surg Br. 2008;90(12):1635–40. https://doi-org/10.1302/0301-620X.90B12.20931.
16. Nelson DG. The influence of carbonate on the atomic structure and reactivity of hydroxyapatite. J Dent Res. 1981;60 Spec No C:1621–9. https://doi-org/10.1177/00220345810600003s1201.
17. Rupani A, Hidalgo-Bastida LA, Rutten F, Dent A, Turner I, Cartmell S. Osteoblast activity on carbonated hydroxyapatite. J Biomed Mater Res Part A. 2012;100A(4):1089–96. https://doi-org/10.1002/jbm.a.34037.
18. Pieters IY, Van den Vreken NM, Declercq HA, Cornelissen MJ, Verbeeck RM. Carbonated apatites obtained by the hydrolysis of monetite: influence of carbonate content on adhesion and proliferation of MC3T3-E1 osteoblastic cells. Acta Biomater. 2010;6(4):1561–8. https://doi-org/10.1016/j.actbio.2009.11.002.
19. Bonel G. Contribution à l'étude de la carbonatation des apatites. Ann Chim. 1972;7:65–88.
20. Fleet ME. Carbonated hydroxyapatite: materials, synthesis, and applications. 1st ed. Jenny Stanford Publishing; 2015.
21. Redey SA, Nardin M, Bernache-Assollant D, Rey C, Delannoy P, Sedel L, et al. Behavior of human osteoblastic cells on stoichiometric hydroxyapatite and type A carbonate apatite: role of surface energy. J Biomed Mater Res. 2000;50(3):353–64. https://doi.org/10.1002/(SICI)1097-4636(20000605)50:3%3C353::AID-JBM9%3E3.0.CO;2-C
22. Li B, Liao X, Zheng L, He H, Wang H, Fan H, et al. Preparation and cellular response of porous A-type carbonated hydroxyapatite nanoceramics. Mater Sci Eng C. 2012;32(4):929–36. https://doi-org/10.1016/j.msec.2012.02.014.
23. Labarthe J-C, Bonnel G, Montel G. Sur la structure et les propriétés des apatites carbonatées de type B phospho-calcique. Ann Chim. 1973;8:289–301.
24. Douard N, Leclerc L, Sarry G, Bin V, Marchat D, Forest V, et al. Impact of the chemical composition of poly-substituted hydroxyapatite ps on the in vitro pro-inflammatory response of macrophages. Biomed Microdevices. 2016;18(2):9. https://doi-org/10.1007/s10544-016-0056-0.
25. Boyer A, Marchat D, Bernache-Assollant D. Synthesis and characterization of Cx-Siy-HA for bone tissue engineering application. Key Eng Mat. 2013;529–530:100–4. https://doi-org/10.4028/www.scientific.net/KEM.529-530.100.
26. Vignoles M, Bonel G, Holcomb DW, Young RA. Influence of preparation conditions on the composition of type-B carbonated hydroxyapatite and on the localization of carbonate ions. Calcified Tissue Inter. 1988;43(1):33–40. https://doi-org/10.1007/BF02555165.
27. Lafon JP, Champion E, Bernache-Assollant D, Gibert R, Danna AM. Thermal decomposition of carbonated calcium phosphate apatites. J Therm Anal Calorim. 2003;72(3):1127–34. https://doi-org/10.1023/A:1025036214044.
28. Lafon JP, Champion E, Bernache-Assollant D. Processing of AB-type carbonated hydroxyapatite Ca10-x(PO4)6–x(CO3)x(OH)2–x-2y(CO3)y ceramics with controlled composition. J Eur Ceram Soc. 2008;28(1):139–47. https://doi-org/10.1016/j.jeurceramsoc.2007.06.009.
29. Rustom LE, Boudou T, Lou S, Pignot-Paintrand I, Nemke BW, Lu Y, et al. Micropore-induced capillarity enhances bone distribution in vivo in biphasic calcium phosphate scaffolds. Acta Biomater. 2016;44:144–54. https://doi-org/10.1016/j.actbio.2016.08.025.
30. Davison NL, Luo X, Schoenmaker T, Everts V, Yuan H, Barrère-de Groot F, et al. Submicron-scale surface architecture of tricalcium phosphate directs osteogenesis in vitro and in vivo. Eur Cell Mater. 2014;27:281–97. https://doi-org/10.22203/ecm.v027a20.
31. Zhang J, Barbieri D, ten Hoopen H, de Bruijn JD, van Blitterswijk CA, Yuan H. Microporous calcium phosphate ceramics driving osteogenesis through surface architecture. J Biomed Mater Res A. 2015;103(3):1188–99. https://doi-org/10.1002/jbm.a.35272.

32. Bouet G, Marchat D, Cruel M, Malaval L, Vico L. In vitro three-dimensional bone tissue models: from cells to controlled and dynamic environment. Tissue Eng Part B Rev. 2015;21(1):133–56. https://doi-org/10.1089/ten.teb.2013.0682.
33. Murphy WL, McDevitt TC, Engler AJ. Materials as stem cell regulators. Nat Mater. 2014;13(6):547–57. https://doi-org/10.1038/nmat3937.
34. Davison NL, Su J, Yuan H, van den Beucken JJ, de Bruijn JD, Barrère-de GF. Influence of surface microstructure and chemistry on osteoinduction and osteoclastogenesis by biphasic calcium phosphate discs. Eur Cell Mater. 2015;29:314–29. https://doi-org/10.22203/ecm.v029a24.
35. Trombe JC, Montel G. Some features of the incorporation of oxygen in different oxidation states in the apatitic lattice—II On the synthesis and properties of calcium and strontium peroxiapatites. J Inorg Nucl Chem. 1978;40(1):23–6. https://doi-org/10.1016/0022-1902(78)80299-1.
36. Seuter AMJH. Existence region of calcium hydroxyapatite and the equilibrium with coexisting phases at elevated temperatures. In: Anderson JSRM, Stone FS, editors. Reactivity of solids. London: Chapman et Hall; 1972.
37. Raynaud S, Champion E, Bernache-Assollant D. Calcium phosphate apatites with variable Ca/P atomic ratio II. Calcination and sintering. Biomaterials. 2002;23(4):1073–80. https://doi-org/10.1016/S0142-9612(01)00219-8.
38. Zhou J, Zhang X, Chen J, Zeng S, De Groot K. High temperature characteristics of synthetic hydroxyapatite. J Mater Sci Mater Med. 1993;4(1):83–5. https://doi-org/10.1007/BF00122983.
39. Locardi B, Pazzaglia UE, Gabbi C, Profilo B. Thermal behaviour of hydroxyapatite intended for medical applications. Biomaterials. 1993;14(6):437–41. https://doi-org/10.1016/0142-9612(93)90146-s.
40. Van Landuyt P, Li F, Keustermans JP, Streydio JM, Delannay F, Munting E. The influence of high sintering temperatures on the mechanical properties of hydroxylapatite. J Mater Sci Mater Med. 1995;6(1):8–13. https://doi-org/10.1007/BF00121239.
41. Adolfsson E, Nygren M, Hermansson L. Decomposition mechanisms in aluminum oxide-apatite systems. J Am Ceram Soc. 1999;82(10):2909–12. https://doi-org/10.1111/j.1151-2916.1999.tb02176.x.
42. Riboud PV. Composition et stabilité des phases à structure d'apatite dans le système CaO-P2O5-oxyde de fer-H2O à haute température. Ann Chim. 1973;8:381–90.
43. Alberius-Henning P, Adolfsson E, Grins J, Fitch A. Triclinic oxy-hydroxyapatite. J Mater Sci. 2001;36(3):663–8. https://doi-org/10.1023/A:1004876622105.
44. Yoder CH, Pasteris JD, Worcester KN, Schermerhorn DV. Structural water in carbonated hydroxylapatite and fluorapatite: confirmation by solid state 2H NMR. Calcified Tissue Int. 2012;90(1):60–7. https://doi-org/10.1007/s00223-011-9542-9.
45. Wang T, Dorner-Reisel A, Müller E. Thermogravimetric and thermokinetic investigation of the dehydroxylation of a hydroxyapatite powder. J Eur Ceram Soc. 2004;24(4):693–8. https://doi-org/10.1016/S0955-2219(03)00248-6.
46. Rey C, Collins B, Goehl T, Dickson IR, Glimcher MJ. The carbonate environment in bone mineral: a resolution-enhanced Fourier Transform Infrared Spectroscopy study. Calcified Tissue Int. 1989;45(3):157–64. https://doi-org/10.1007/BF02556059.
47. Charbonnier B. Développement de procédés de mise en forme et de caractérisation pour l'élaboration de biocéramiques en apatites phosphocalcique carbonatées. Univ Lyon; 2016.
48. Liao CJ, Lin FH, Chen KS, Sun JS. Thermal decomposition and reconstitution of hydroxyapatite in air atmosphere. Biomaterials. 1999;20(19):1807–13. https://doi-org/10.1016/S0142-9612(99)00076-9.
49. Wilson EE, Awonusi A, Morris MD, Kohn DH, Tecklenburg MMJ, Beck LW. Three structural roles for water in bone observed by solid-state NMR. Biophys J. 2006;90(10):3722–31. https://doi-org/10.1529/biophysj.105.070243.
50. Pajchel L, Kolodziejski W. Solid-state MAS NMR, TEM, and TGA studies of structural hydroxyl groups and water in nanocrystalline apatites prepared by dry milling. J Nanopart Res. 2013;15(8):1868. https://doi-org/10.1007/s11051-013-1868-y.
51. Nowicki DA, Skakle JMS, Gibson IR. Faster synthesis of A-type carbonated hydroxyapatite powders prepared by high-temperature reaction. Adv Powder Technol. 2020;31(8):3318–27. https://doi-org/10.1016/j.apt.2020.06.022.

52. LeGeros RZ, Trautz OR, Klein E, LeGeros JP. Two types of carbonate substitution in the apatite structure. Cell Mol Life Sci. 1969;25(1):5–7. https://doi-org/10.1007/bf01903856.
53. Driessens FCM, Verbeeck RMH, Heijligers HJM. Some physical properties of Na- and CO3-containing apatites synthesized at high temperatures. Inorg Chim Acta. 1983;80:19–23. https://doi-org/10.1016/S0020-1693(00)91256-8.
54. Barralet JE, Fleming GJP, Campion C, Harris JJ, Wright AJ. Formation of translucent hydroxyapatite ceramics by sintering in carbon dioxide atmospheres. J Mater Sci. 2003;38(19):3979–93. https://doi-org/10.1023/A:1026258515285.
55. Jebri S, Khattech I, Jemal M. Standard enthalpy, entropy and Gibbs free energy of formation of «A» type carbonate phosphocalcium hydroxyapatites. J Chem Thermodyn. 2017. https://doi-org/10.1016/j.jct.2016.10.035.
56. Vieillard P, Tardy Y. Thermochemical Properties of Phosphates. In: Nriagu JO, Moore PB, editors. Phosphate minerals. Berlin: Springer; 1984. p. 171–98. https://doi-org/10.1007/978-3-642-61736-2_4.